

DARK MOLECULAR GAS IN SIMULATIONS OF $Z \sim 0$ DISC GALAXIES

QI LI,¹ DESIKA NARAYANAN,^{1,2,3} ROMEEL DAVÈ,^{4,5,6} AND MARK R. KRUMHOLZ^{7,8}

¹*Department of Astronomy, University of Florida, 211 Bryant Space Sciences Center, Gainesville, FL 32611 USA*

²*University of Florida Informatics Institute, 432 Newell Drive, Gainesville, FL 32611 USA*

³*Cosmic Dawn Center (DAWN), Niels Bohr Institute, University of Copenhagen, Juliane Maries vej 30, DK-2100 Copenhagen, Denmark*

⁴*Institute for Astronomy, Royal Observatory, Edinburgh, EH9 3HJ, UK*

⁵*University of the Western Cape, Bellville, Cape Town 7535, South Africa*

⁶*South African Astronomical Observatory, Cape Town 7925, South Africa*

⁷*Research School of Astronomy and Astrophysics, Australian National University, Canberra 2611, A.C.T., Australia*

⁸*Centre of Excellence for Astronomy in Three Dimensions (ASTRO-3D), Australia*

(Received; Revised; Accepted)

Submitted to ApJ

ABSTRACT

The H₂ mass of molecular clouds has traditionally been traced by the CO(J=1-0) rotational transition line. This said, CO is relatively easily photodissociated, and can also be destroyed by cosmic rays, thus rendering some fraction of molecular gas to be “CO-dark”. We investigate the amount and physical properties of CO-dark gas in two $z \sim 0$ disc galaxies, and develop predictions for the expected intensities of promising alternative tracers ([C I] 609 μm and [C II] 158 μm emission). We do this by combining cosmological zoom simulations of disc galaxies with thermal-radiative-chemical equilibrium interstellar medium (ISM) calculations to model the predicted H I and H₂ abundances and CO (J=1-0), [C I] 609 μm and [C II] 158 μm emission properties. Our model treats the ISM as a collection of radially stratified clouds whose properties are dictated by their volume and column densities, the gas-phase metallicity, and the interstellar radiation field and cosmic ray ionization rates. Our main results follow. Adopting an observationally motivated definition of CO-dark gas, i.e. H₂ gas with $W_{\text{CO}} < 0.1$ K-km/s, we find that a significant amount ($\gtrsim 50\%$) of the total H₂ mass lies in CO-dark gas, most of which is diffuse gas, poorly shielded due to low dust column density. The CO-dark molecular gas tends to be dominated by [C II], though [C I] also serves as a bright tracer of the dark gas in many instances. At the same time, [C II] also tends to trace neutral atomic gas. As a result, when we quantify the conversion factors for the three carbon-based tracers of molecular gas, we find that [C I] suffers the least contamination from diffuse atomic gas, and is relatively insensitive to secondary parameters.

1. INTRODUCTION

Star formation as observed in the local Universe occurs exclusively in giant clouds of molecular hydrogen (H_2) (e.g. Kennicutt & Evans 2012; Krumholz 2014; Lada & Lada 2003). While H_2 is the most abundant constituent of these giant molecular clouds (GMCs), its low mass requires temperatures of ~ 500 K to excite the first quadrupole line. As a result, direct H_2 emission from the relatively cold ($T \sim 10 - 30$ K) interstellar clouds is relatively faint.

With a typical abundance of $\sim 10^{-4} \times \text{H}_2$ (Lee et al. 1996), ^{12}CO (hereafter, CO) is the second most abundant molecule in GMCs, and used as a common tracer of the underlying molecular hydrogen. The luminosity from the ground rotational state of CO (CO J=1-0) is typically used to convert to an H_2 mass via a CO- H_2 conversion factor:

$$X_{\text{CO}} = \frac{W_{\text{CO}}}{N_{\text{H}}} \quad (1)$$

where W_{CO} is the velocity integrated CO intensity (in K-km/s), and N_{H} is the H_2 column density.

The value of this CO- H_2 conversion factor is hotly debated (see, the reviews by Bolatto et al. 2013 and Casey et al. 2014). Fundamentally, there are two issues. First, even at a fixed CO abundance, the velocity integrated CO intensity W_{CO} depends on the physical properties (kinetic temperature and velocity dispersion) of the gas (Narayanan et al. 2011, 2012). These vary both within and amongst galaxies, and therefore can drive variations in X_{CO} accordingly (e.g. Feldmann et al. 2012; Shetty et al. 2011a,b). Second, CO can be both photodissociated and destroyed by cosmic rays (CRs) via collisions with He^+ (Bisbas et al. 2015; Narayanan & Krumholz 2017; Gong et al. 2017, 2018). Because of this, there can be molecular gas that is significantly depleted in CO. Understanding the origin and physical properties of this so-called ‘‘CO-dark molecular gas’’ is the main purpose of this investigation.

Indeed, observational studies have uncovered dark molecular gas in the Milky Way and nearby galaxies. The principal methods for characterizing dark gas thus far include the detection of H_2 gas via γ -ray observations (e.g. Grenier et al. 2005), dust continuum emission (e.g. Planck Collaboration et al. 2011) and $\text{C}^+ 158\mu\text{m}$ emission (Pineda et al. 2013, 2014; Langer et al. 2014b,a). Defining gas with CO intensity weaker than some threshold as CO-dark, these methods have found that as much as $\sim 30 - 70\%$ of the molecular gas in the Galaxy may be in a CO-dark phase.

Potential tracers of CO dark molecular gas include the [C I] $^3\text{P}_1 \rightarrow ^3\text{P}_0$ $609\mu\text{m}$ line, and the [C II] $^3\text{P}_{3/2} \rightarrow ^3\text{P}_{1/2}$ $158\mu\text{m}$ line. Both C I and C^+ are natural byproducts of the ultraviolet-induced photodissociation of CO, or cosmic-ray driven ion-neutral reaction (e.g. Bisbas et al. 2015; Narayanan & Krumholz 2017). C^+ can be excited by collisions with a variety of partners, i.e. electrons, H I, and H_2 (Goldsmith et al. 2012; Herrera-Camus et al. 2015). Because it can be excited by collisions with all these partners, and because the low ionization potential of C (11.3 eV) renders C^+ the dominant form of carbon in most of the neutral

ISM, [C II] emission can arise from nearly every phase of the ISM. This said, Pineda et al. (2014) used Herschel observations to constrain the origin of the bulk of Galactic [C II] emission as coming from molecular gas. Similarly, Olsen et al. (2015) suggested (via numerical simulations) that this is likely true even for $z \sim 2$ main sequence galaxies. Even so, at lower metallicities, the fraction of [C II] emission that originates from ionized gas may increase (Olsen et al. 2017).

Similarly, the [C I] $^3\text{P}_1 \rightarrow ^3\text{P}_0$ transition line has an excitation potential ~ 23.6 K, and can therefore be excited in typical molecular clouds. Observational studies have shown spatial correlation with both low-J CO emission and H_2 abundances (Papadopoulos & Greve 2004; Bell et al. 2007; Walter et al. 2011; Israel et al. 2015). Bothwell et al. (2017) show similar [C I] and CO linewidths of a range of high- z galaxies. Those observations span a wide range of environments, from local molecular clouds to high redshift (U)LIRGS, implying that [C I] may be able to trace the gas component traditionally traced by CO emission.

The results from theoretical models are mixed. With respect to [C II], theoretical studies have typically focused on disentangling different components of [C II] emission. Utilizing hydrodynamics simulations of star formation regions combined with photodissociation region (PDR) and radiative transfer modeling, Accurso et al. (2017) find that $\sim 60-80\%$ of [C II] comes from molecular regions, depending mainly on the specific star formation rate. Similarly, Olsen et al. (2017) found $\sim 66\%$ of [C II] comes from molecular gas in star forming galaxies at $z \sim 6$. Using a kpc-scale patch extracted from isolated galaxies, Glover & Smith (2016) found a weak correlation between the [C II] intensity and N_{H} .

On the other hand, [C I] has been historically interpreted as only a tracer of surface layer of a thin PDR layer on the surface of clouds (e.g. Tielens & Hollenbach 1985). This interpretation was questioned in subsequent studies. For example, Papadopoulos et al. (2004) suggested that [C I] can be widespread in molecular regions traditionally traced by CO emission, due to increased exposure to interstellar radiation fields from turbulence (Xie et al. 1995; Spaans & van Dishoeck 1997; Cubick et al. 2008).

A number of groups have investigated the behavior of [C I] in smaller scale molecular cloud simulations (Offner et al. 2014; Glover et al. 2015). They point out several advantages of C I over CO: the column density regime of [C I] where the corresponding conversion factor $X_{\text{C I}}$ remains approximately constant is larger, and $X_{\text{C I}}$ is less sensitive to secondary parameters such as interstellar radiation field strength.

Thus far, what has been missing is an investigation into the expected fraction of CO-dark molecular gas on galaxy-wide scales. Understanding this is the focus of the present paper. To do this, we take advantage of a combination of cosmological zoom-in simulations with thermal-radiative-chemical equilibrium interstellar medium (ISM) calculations to model

the predicted H_2 , H I , $\text{CO}(1-0)$, $[\text{C I}]$ and $[\text{C II}]$ emission¹ from giant clouds in galaxy simulations. Here, we focus on $z \sim 0$ disc galaxies, though we plan to extend our models to galaxy populations at high-redshift in subsequent work. In this paper, we ask three fundamental questions:

1. How much CO-dark molecular gas is there in $z \sim 0$ disc Galaxies?
2. What are the physical properties of this dark molecular gas?
3. What are the best alternative tracers of CO-dark gas?

In §2, we summarize our simulation methods. In §3, we show sample results from simplified cloud based on our modeling to develop our physical intuition. In §4, we investigate the amount and properties of CO-dark molecular gas, and examine the utility of different carbon-based tracers. In §6, we then discuss our results in the context of other relevant theoretical studies and the sensitivity of uncertain parameters in our model. We summarize in §7.

2. METHODS

2.1. Cosmological Zoom Galaxy Formation Simulations

We examine two Milky Way-like galaxies formed in cosmological zoom-in simulations using the MUFASA physics suite (Davé et al. 2016, 2017a,b). The basic physics in these simulations is described in Narayanan et al. (2018a,b) and Privon et al. (2018), and we refer the reader to these papers for details, though summarize the salient points here.

We first simulate a 50 Mpc^3 dark matter only box at relatively low mass resolution ($M_{\text{DM}} = 7.8 \times 10^8 h^{-1} M_{\odot}$) down to redshift $z = 0$. We conduct this (and our main zoom in simulation) with the hydrodynamic code GIZMO in Meshless Finite Mass (MFM) mode (Hopkins 2015, 2017). We employ the cubic spline kernel with 64 neighbors, which leads to a minimum smoothing length $\epsilon \sim 30 \text{ pc}$. We evaluate volume and column densities of gas on the scale of the smoothing length. Our initial conditions are generated with MUSIC (Hahn & Abel 2011), and are exactly the same as the MUFASA cosmological hydrodynamic simulation series (Davé et al. 2016, 2017a,b).

From the $z = 0$ snapshot, we identify dark matter halos with CAESAR (Thompson et al. 2014), and select 2 halos with dark matter halo masses $M_{\text{halo}} = 1.9 \times 10^{12} M_{\odot}$ and $2.1 \times 10^{12} M_{\odot}$. These are named ‘‘Halo 352’’ and ‘‘Halo 401’’ respectively, hereafter. We identify all particles within $2.5 \times r_{\text{max}}$, where r_{max} is the distance of the particle with maximum radius from the halo center of mass at $z = 0$. We track these particles back to redshift $z = 249$, and split them

in order to achieve higher mass resolution. At this point, we also add baryons according to the cosmic baryon fraction. Our final particle masses are $M_{\text{DM}} = 1 \times 10^6 h^{-1} M_{\odot}$, and baryon mass $M_{\text{b}} = 1.9 \times 10^5 h^{-1} M_{\odot}$.

We re-run these higher-resolution simulations from an initial redshift $z = 249$ down to $z = 0$. Our galaxy formation physics follows that employed in the MUFASA cosmological hydrodynamic simulation. We refer the reader to Davé et al. (2016) for a detailed description of these models. Briefly, we use the GRACKLE-3.1 chemistry and cooling library (Smith et al. 2017), which includes primordial and metal-line cooling. Gas is allowed to cool down to 10^4 K , below which it is pressurized in order to resolve Jeans mass. Stars form in molecular gas, where the H_2 fraction is calculated following the Krumholz et al. (2009) methodology. We impose a minimum value of metallicity $Z = 10^{-3} Z_{\odot}$ entering the calculation. We take this floor value from Kuhlen et al. (2012), who show that a minimum metallicity of this order should be produced by metal enrichment from population III stars, which form in early halos with masses well below the resolution limit of our simulations. The rate of star formation proceeds following a volumetric Schmidt (1959) relation, with an enforced efficiency per free fall time of $\epsilon_{\text{ff}} = 0.02$ as motivated by observations (e.g. Kennicutt 1998; Kennicutt & Evans 2012; Krumholz et al. 2012; Narayanan et al. 2012; Vutisalchavakul et al. 2016; Heyer et al. 2016; Leroy et al. 2017).

These stars drive winds in the interstellar medium. This form of feedback is modeled as a two-phase decoupled wind. The modeled winds have an ejection probability that scales with both the SFR and the galaxy circular velocity (a quantity calculated on the fly via fast friends-of-friends galaxy identification). The nature of these scaling relations follow the results from higher-resolution studies in the Feedback In Realistic Environments zoom simulation campaign (e.g. Muratov et al. 2015; Hopkins et al. 2014, 2017). We additionally include feedback from longer-lived stars (e.g. asymptotic giant branch stars and Type Ia supernovae) following Bruzual & Charlot (2003) stellar evolution tracks with a Chabrier (2003) initial mass function. MUFASA also includes an additional, artificial ‘‘quenching feedback’’ intended to suppress star formation in massive halos, but we do not use it in the simulations presented in this paper because our halos are below mass threshold where it applies.

Metal enrichment yields for type Ia and type II supernovae are drawn from Iwamoto et al. (1999) and Nomoto et al. (2006), respectively (though note that the latter yields are reduced by a factor 50% to match the mass-metallicity relation statistically, following the discussion in Davé et al. 2016). Asymptotic Giant Branch (AGB) star yields are drawn from Oppenheimer & Davé (2006).

The results of these simulations are 2 disc-like galaxies at redshift $z = 0$. In Figure 1, we show the gas surface density images of one of our model galaxies from $z = 5$ to 0, and list the final physical properties of these galaxies in Table 1. Figure 2 shows where the simulated galaxies are located in the mass-metallicity plane. Compared against the

¹ Because we refer to both abundances and intensities in this paper, we must be a bit careful with our terminology. We hereafter refer to CO (J=1-0) emission as CO (1-0), while we refer to the molecule itself as ‘‘CO’’. We refer to $[\text{C I}] \ ^3\text{P}_1 \rightarrow \ ^3\text{P}_0$ emission as $[\text{C I}]$, while we refer to the neutral atom itself as ‘‘C I’’. Finally, we refer to $[\text{C II}] \ 158\mu\text{m}$ emission as $[\text{C II}]$, while we refer to singly ionized carbon as C^+ .

Table 1. Zoom Simulation Summary

Halo ID	$M_{\text{DM}}(z=0)$	$M_*(z=0)$	$M_{\text{g,HI+H}_2}(z=0)$	SFR
	M_\odot	M_\odot	M_\odot	$M_\odot \text{ yr}^{-1}$
mz352	1.9×10^{12}	3.3×10^{10}	1.3×10^{10}	3.8
mz401	2.1×10^{12}	2.6×10^{10}	4.2×10^{10}	4.3

NOTE—Halo ID number, halo mass, stellar mass, neutral gas (H I + H₂) mass and SFR. All physical quantities are calculated at $z = 0$

mass-metallicity relation (Tremonti et al. 2004), our galaxies have only slightly lower gas metallicity, which could lead to a smaller amount of CO-bright gas. Abruzzo et al. (2018) show the location of these galaxies on both the SFR- M_* relation, as well as the M_* - M_{halo} relation.

2.2. Computation of Thermal States, Chemical States and Line Emission

We calculate the chemical abundances and line emission of the gas through post-processing the gas particles from the simulated galaxy. We utilize the code Derive the Energetics and Spectra of Optically Thick Interstellar Clouds (DESPOTIC; Krumholz 2014) to compute the chemical state, temperature and level populations in each layer. We briefly summarize the computation here, and refer readers interested in further details to Krumholz (2014) and Narayanan & Krumholz (2017).

The computation of emergent luminosity requires three steps: calculating thermal equilibrium, chemical equilibrium, and statistical equilibrium. In practice, these three steps are done iteratively. To perform these, we first assume that every particle is a sphere, and is radially stratified into 8 concentric zones. Note, we test the convergence by varying the number of zones from 8 to 64, and show in Appendix that the 8-zone model is sufficient to produce a converged result. The equilibrium calculations for each zone is done independently from one another.

Each particle has a density ρ , and particle mass M known from the hydrodynamic simulations. We assign the column density of H nuclei $N_H = (3/4) \Sigma_g / \mu_H$ where μ_H is the mean molecular weight. The factor 3/4 is the difference between mean column density and center-to-edge column density. Within each zone, we adopt total abundances of [C/H] = $2 \times 10^{-4} Z'$ consistent with their Milky Way abundances (Lee et al. 1996; Draine 2011). Here, Z' is the metallicity scaled to a solar value of 0.0134 (Asplund et al. 2009).

We model the chemical state of each zone using the reduced carbon-oxygen chemical network as developed by Nelson & Langer (1999), combined with the Glover & Mac Low (2007) non-equilibrium hydrogen chemical network (hereafter NL99+GC). The reaction rates and full network are described in detail in Table 2 of Narayanan & Krumholz

(2017). This network specifies the fraction of carbon in CO, C I and C⁺ in each zone, as well as H I and H₂.

This network requires that we specify the strength of the unshielded interstellar radiation field (ISRF), which we characterize in terms of the far-ultraviolet radiation field. We normalize this field to the solar neighborhood value χ_{FUV} , which we assume is linearly proportional to the total galaxy SFR. The normalization of this scale is set to $1 M_\odot \text{ yr}^{-1}$, based on the approximate observed Milky Way value (Rorbitaille & Whitney 2010; Chomiuk & Povich 2011).

We additionally must specify the amount by which we reduce the rates of all photochemical reactions by dust shielding in the interiors of clouds. We characterize this dust-shielding in terms of the visual extinction $A_v = (1/2) (A_v/N_H) N_H$, where the ratio of (A_v/N_H) is the dust extinction per H nucleus at V band, and the factor of 1/2 represents the rough average column over the entire volume of the cloud. The reduction in the H₂ dissociation rate is evaluated using the Draine & Bertoldi (1996) shielding function, and the reduction in CO photodissociation is determined using an interpolated version of the shielding function of van Dishoeck & Black (1988).

We further specify a cosmic ray (CR) ionization rate. Recent observations suggest the CR ionization rate $\xi \sim 10^{-16} \text{ s}^{-1}$ in the diffuse ISM (Neufeld et al. 2010; Indriolo et al. 2015; Neufeld & Wolfire 2017). However, considering that a significant amount of the CR flux is at low energies, the ionization rate in the interiors of molecular clouds will likely be lower due to shielding. Similarly, the relatively large values of $\xi \sim 10^{-16} \text{ s}^{-1}$ are at tension with the low inferred temperatures of typical molecular clouds (e.g. Narayanan et al. 2011; Narayanan & Davé 2012). Because of this, we adopt a more conservative value of $\xi = 10^{-17} \text{ s}^{-1}$. We assume that the CR ionization rate ξ scales linearly with the SFR, i.e. $\xi = 10^{-17} \text{ SFR}/M_\odot \text{ yr}^{-1} \text{ s}^{-1}$. Note, increasing this value will have the effect of increasing the CO-dark fraction in clouds.

Alongside our chemical equilibrium calculations, we determine the thermal state of each zone of our model clouds. To do this, we follow Goldsmith (2001) and Krumholz et al. (2011) in balancing the relevant heating and cooling processes. The heating processes we consider are the cosmic microwave background (CMB) (set to $T_{\text{CMB}} = 2.73 \text{ K}$), heating of the dust by the ISRF, heating of the dust by a background thermal infrared field with an effective temperature of 10K, grain photoelectric heating in the gas, and cosmic ray heating of the gas. The cooling processes are dominated by line cooling of the gas by C⁺, C I, O and CO, as well as of atomic hydrogen excited by electrons via the Ly α and Ly β lines (processes that can be relevant at $T \gtrsim 5000 \text{ K}$, which is possible in the outskirts of our clouds). There is additionally an energy exchange between gas and dust.

Finally statistical equilibrium is assumed to determine the level populations of each species. DESPOTIC uses the escape probability approximation for the radiative transfer problem, where f_i , the fraction of each species in quantum state i is

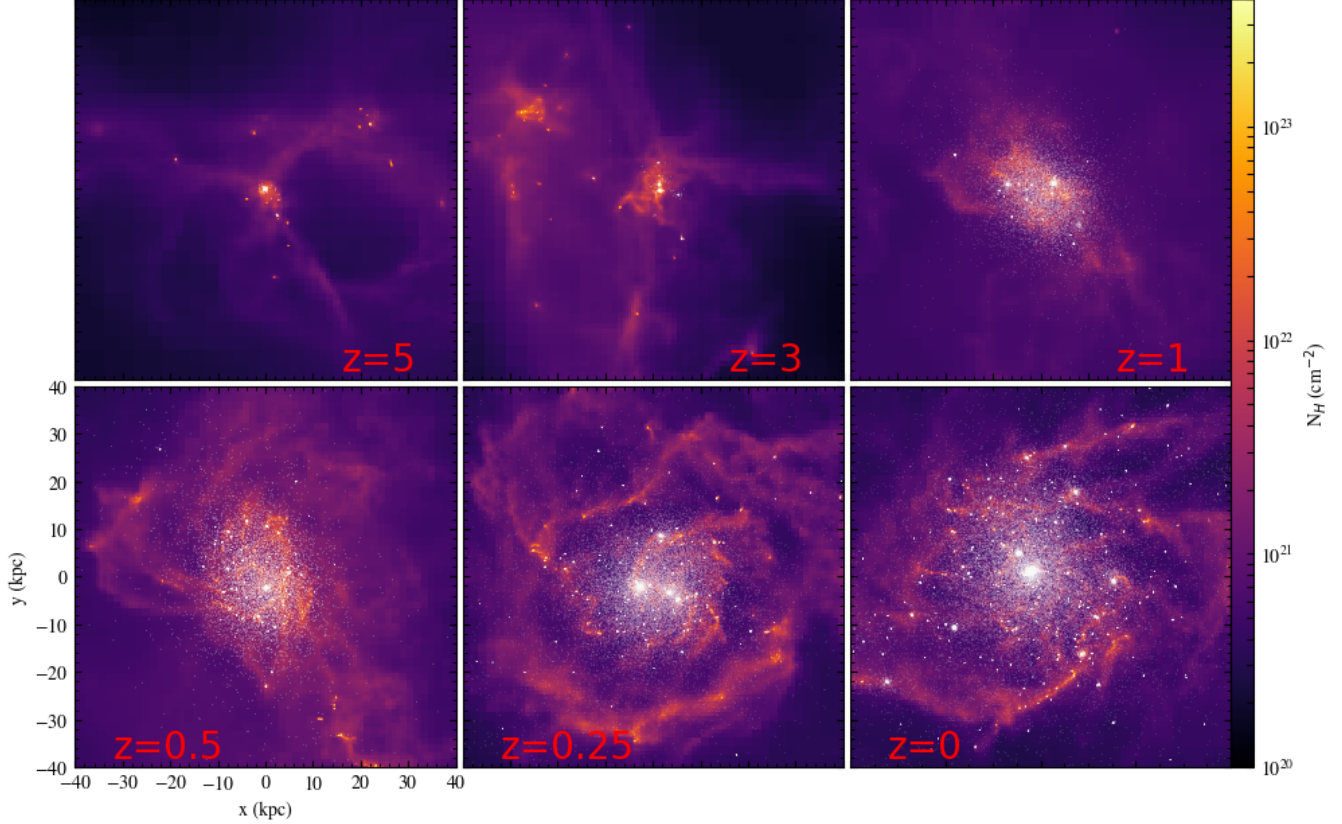


Figure 1. Gas surface density projection maps of in formation from redshifts $z = 6$ to 0 . The panels are 80 kpc (comoving) on a side, and the color scale is common for all images with the color scale on the right. The star particles are overplotted to show the stellar disks.

computed solving the linear system of equations

$$\begin{aligned} & \sum_j f_j \left[q_{ji} + \beta_{ji}(1 + n_{\gamma,ji})A_{ji} + \beta_{ij} \frac{g_i}{g_j} n_{\gamma,ij} A_{ij} \right] \\ & = f_i \sum_k \left[q_{ik} + \beta_{ik}(1 + n_{\gamma,ik})A_{ik} + \beta_{ki} \frac{g_k}{g_i} n_{\gamma,ki} A_{ki} \right] \end{aligned} \quad (2)$$

where $\sum_i f_i = 1$, A_{ij} are the usual Einstein coefficients for spontaneous emission (from $i \rightarrow j$), g_i, g_j are the degeneracies of the states,

$$n_{\gamma,ij} = \frac{1}{\exp(\Delta E_{ij}/k_B T_{\text{CMB}}) - 1} \quad (3)$$

is the photon occupation number of the CMB, E_{ij} is the energy difference between states i and j , and β_{ij} is the es-

cape probability for photons of this energy (Draine 2011). q_{ij} are the collisional transition rates between states, where the calculation of collision rates includes both H I and H₂, in proportion to their abundances as determined by the chemical network. The Einstein and collisional rate coefficients all come from the Leiden Atomic and Molecular Data Base (LAMADA; Schöier et al. 2005; Jankowski & Szalewicz 2005; Wernli et al. 2006; Yang et al. 2010; Launay & Roueff 1977; Johnson et al. 1987; Roueff & Le Bourlot 1990; Schroder et al. 1991; Staemmler & Flower 1991; Barinovs et al. 2005; Wilson & Bell 2002; Flower & Launay 1977; Flower 1988, 2001; Lique et al. 2013; Wiesenfeld & Goldsmith 2014).

To compute the chemical and thermal states, alongside the emergent line luminosity, we first guess an initial tempera-

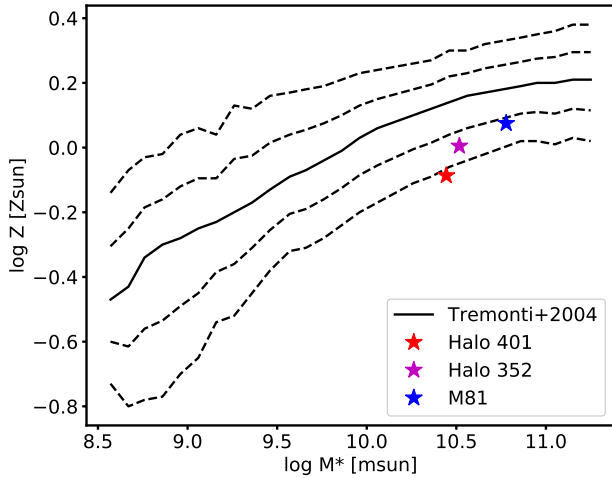


Figure 2. The mass-metallicity relation (solid line, with dashed lines representing 1σ and 2σ uncertainties; Tremonti et al. 2004). The red stars denote the mass-weighted metallicity of molecular gas versus stellar mass in our simulated galaxies (Halo 401 and Halo 352). The blue star denotes M81 (Kudritzki et al. 2012)

ture, chemical state and level populations for each layer in the cloud. We then iterate each process in each zone independently. The outermost loop is the chemical network, and this is run to convergence while holding the temperature fixed. The middle loop computes the temperature, holding the level populations fixed. Finally, the innermost loop (the level populations) are iterated for each species to convergence. We iterate in this manner until the chemical abundances, temperatures, and level populations are converged. With these in hand, the total line luminosity per unit mass in each zone is summed.

Finally, we note that this process is computationally expensive. When considering the relatively large number of gas particles in a single snapshot, it is prohibitive to determine the line luminosity in this manner on a particle-by-particle basis. Because of this, we have built a 4-dimensional lookup table where we compute the aforementioned DESPOTIC calculations in a fine grid over a range of n_{H} , N_{H} , star formation rates and metallicity. The lookup table spans the metallicity, column density, volume density, and SFR space of $0.1 \leq Z' \leq 1.5$, $1 \leq n_{\text{H}} \leq 10^4$, $1 \leq N_{\text{H}}/(M_{\odot}/\text{pc}^2) \leq 10^4$, and $1 \leq \text{SFR}/(M_{\odot}/\text{yr}) \leq 10^3$. The spacing of the grid is 0.28, 0.2 dex, 0.2 dex, 0.15 dex for Z' , n_{H} , N_{H} and SFR, respectively. The results presented here are all converged with respect to the grid resolution of the lookup tables.

3. DEVELOPING INTUITION: RESULTS FROM SIMPLIFIED CLOUD MODELS

Before we explore our main results, it is worth first going through a pedagogical exploration of the chemical properties of individual spherical, radially stratified DESPOTIC clouds.

These numerical experiments will allow us to develop a physical intuition that will be useful when examining the CO, C I and C⁺ abundances in bona fide galaxy zoom simulations.

For the purpose of the idealized numerical experiments we develop in this section, we fix the initial density of spherical clouds to $n_{\text{H}} = 100 \text{ cm}^{-3}$ and run the chemical–thermal–statistical network to equilibrium. In Figure 3, we examine the relationship between the CO, C I and C⁺ abundances as a function of column density when varying the star formation rate (SFR; upper panel) and metallicity (lower panel). We overplot the H₂ and H I abundances which are normalized to unity instead of 2×10^{-4} and a +1 offset to show how H₂ fractional abundances are impacted by SFR and metallicity.

With fixed SFR and metallicity, the H₂ abundance increases as the column density increases, mainly due to the increased ability of hydrogen to self-shield against the photodissociating radiation. At a fixed column density, the H₂ abundance also increases as the metallicity increases, owing to the increased efficacy of dust shielding. Conversely, a higher SFR (which results in a stronger photo-dissociating FUV field and cosmic-ray ionization rate) tends to reduce the H₂ abundance.

For a fixed set of physical conditions (i.e. SFR and Z'), C⁺ tends to dominate the low column density regime (here, the outskirts of our spherical clouds) while CO dominates the high column density regime. As we show in the upper panel of Figure 3, at a fixed SFR, carbon tends to transition from ionized form to molecular with increasing metallicity due to enhanced dust shielding.

Compared to the hydrogen abundances, the transition of carbon species’ composition occurs at higher column densities due to the lack of self-shielding. The SFR has a much more significant effect on the abundances of carbon in different phases. Enhanced SFRs slightly expand the C⁺-dominated region while significantly enlarging the C I-dominated region. This is mainly due to the fact that CO, unlike H₂, is unable to self-shield. Its survival is therefore more sensitive to FUV photo-dissociation, as well as destruction via cosmic rays (via a two-body reaction from ionized He⁺, Bisbas et al. 2015; Narayanan & Krumholz 2017).

4. CO-DARK GAS IN COSMOLOGICAL GALAXY FORMATION SIMULATIONS

We now turn our attention to understanding the utility of different carbon-based tracers of molecular gas in the cosmological zoom simulations of Milky Way analogs. We frame these results in terms of answering a number of specific questions of interest. We assume for both models an SFR of $1M_{\odot}/\text{yr}$ for snapshots analyzed in this paper. This is comparable to the actual SFRs, though it is cleaner when comparing results across multiple models to impose a constant SFR.

5. DEFINITIONS

We begin the analysis of our results with some definitions. Motivated by observations, we define CO-dark gas as H₂ gas layer with $\bar{W}_{\text{CO}} < 0.1 \text{ K-km/s}$. This value matches the typical sensitivity in observations of nearby molecular clouds

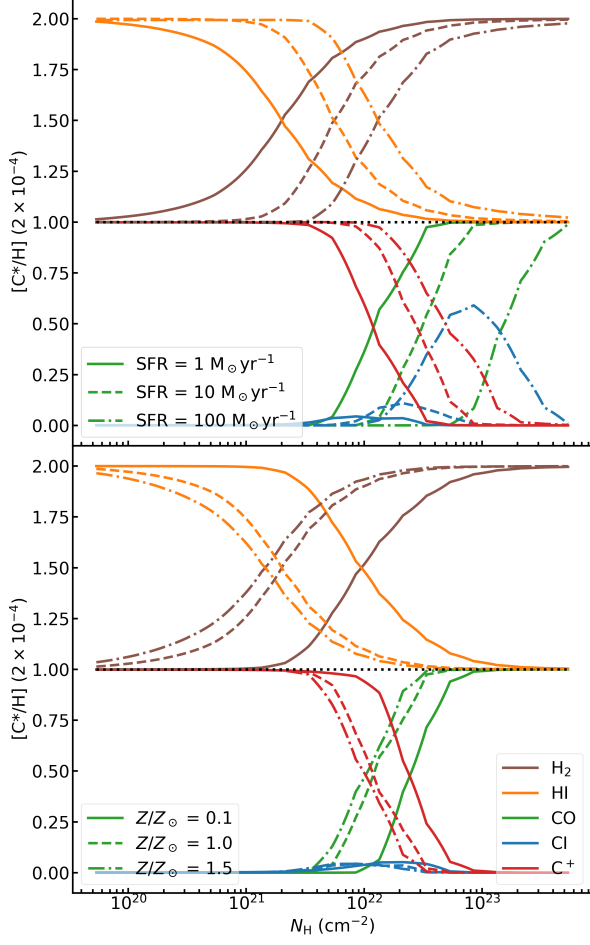


Figure 3. Carbon species’ abundances from idealized cloud models with a fixed density $n_{\text{H}} = 100 \text{ cm}^{-3}$. Upper panel: $[\text{C}^*/\text{H}]$ as functions of N_{H} . We fix the metallicity to solar. We vary the star-formation-rate to values of $\text{SFR} = 1$ (solid line), 10 (dashed line), 100 M_{\odot}/yr (dotted dashed line). Lower panel: CO (green), C I (blue), C^+ (red) abundances with regard to H ($[\text{C}^*/\text{H}]$) as functions of N_{H} . We fix the star formation rate to $\text{SFR} = 1 M_{\odot}/\text{yr}$. We vary the metallicity to values of $Z'/Z_{\odot} = 0.1$ (solid line), 1.0 (dashed line), 1.5 (dotted dashed line). We overplot the hydrogen species’ abundances which are normalized to unity instead of 2×10^{-4} and a +1 offset.

(e.g. Pineda et al. 2008; Smith et al. 2012; Ripple et al. 2013; Leroy et al. 2016).

When examining properties of CO-dark gas and the utility of different tracers, we only consider gas with $W_{\text{CO}} > 10^{-5}$ K-km/s. As will be shown later in Figure 9, only $\sim 10\%$ of H_2 mass associated with gas fainter than this limit, which is extremely diffuse, atomic or ionized. In this type of gas, H_2 can only exist sparsely in dense substructures well below the model resolution (even the finest resolution of observations). As a result, the emission calculated from our model, which is an average of a whole layer, cannot represent the emission

from real H_2 regions, and is therefore not interesting to discuss.

Because our radially stratified clouds are comprised of a mixture of H I and H_2 , to simplify our presentation of results, we refer to layers of our clouds as “molecular” if $M_{\text{H}_2}/M_{\text{HI}+\text{H}_2} \geq 0.5$ and “atomic” if $M_{\text{H}_2}/M_{\text{HI}+\text{H}_2} < 0.5$.

5.1. Where Does CO(1-0), [C I] and [C II] Emission Come from?

We first examine what fractions of emission of CO(1-0), [C I] and [C II] come from molecular versus atomic gas.

In the upper row of Figure 4, we show three panels, each showing the probability distribution functions (PDFs) of CO, C I and C^+ (left to right) abundances for our two model galaxies at redshift $z = 0$. For both galaxies, CO does not exist in any appreciable abundance in atomic gas, nor does C I. Rather, both principally reside in molecular H_2 gas. On the other hand, C^+ can reside in both atomic and molecular gas, and the carbon in atomic gas is almost exclusively in the ionized C^+ phase.

Correspondingly, in the lower row of Figure 4, we show three panels, each showing the PDFs of the intensity from CO(1-0), [C I] and [C II] (left to right) coming from both atomic and molecular gas. The orange line in each panel shows the distribution of line intensities (K-km/s) that come from atomic gas, while the green line shows the distribution of line intensities that come from molecular gas. As we transition from molecular (CO 1-0) to atomic ([C I]) to ionized ([C II]) carbon emission, the fraction of emission that originates in molecular gas decreases, and the fraction that originates in atomic gas increases.

We quantify the mass fraction of molecular gas dominated by CO (1-0), [C I] and [C II]. For example, CO (1-0) is classified as dominating when the CO (1-0) intensity (in $\text{erg s}^{-1} \text{ cm}^{-2} \text{ sr}^{-1}$) is greater than either [C I] or [C II]. Nearly 80% of the molecular gas is dominated by [C II], while the bulk of the remainder is dominated by CO (1-0). The fraction of molecular gas dominated by [C I] emission is negligible; this owes to the relatively narrow set of physical conditions in which [C I] emission peaks (c.f. Figure 3). This said, this should not be interpreted as [C I] being an ineffective tracer of molecular gas. Rather, even if [C I] is mostly fainter than [C II], it is still brighter than CO(1-0) in the CO-dark gas. In fact, as we will show in § 5.3, [C I] emission is generally strong enough and can serve as a reasonably reliable tracer of H_2 gas.

5.2. What Are the Physical Properties of CO-dark Gas?

Having established that a significant fraction of the molecular gas in $z \sim 0$ disc galaxies is CO-dark, we next investigate the physical properties of this gas.

In Figure 5, we show the CO(1-0) intensity of molecular gas of an example galaxy (the $z = 0$ snapshot of model Halo 401) as a function of cloud column density (N_{H}) and gas metallicity (note, Halo 352 has a similar result). We show these two variables as they are critical, as a combination, to shield CO from photodissociating Lyman-Werner band

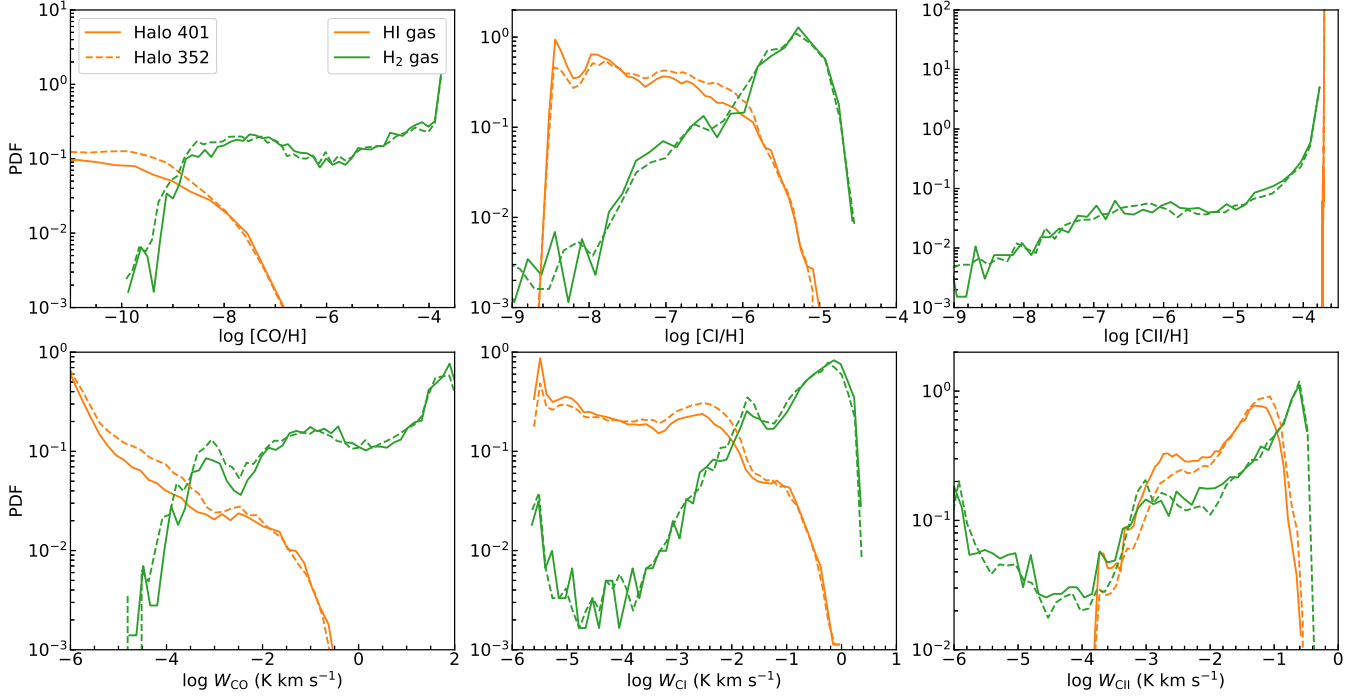


Figure 4. Upper row: PDFs of CO, C I and C⁺ abundances (from left to right) in molecular gas (H₂ abundance > 0.5; green) and atomic gas (HI abundance > 0.5; orange) for Halo 401 and Halo 352 at redshift $z = 0$. CO does not exist in any appreciable abundance in atomic gas, nor does C I. Rather, both principally reside in molecular H₂ gas. On the other hand, C⁺ can reside in both atomic and molecular gas, and carbon in atomic gas is almost exclusively in the ionized C⁺ phase, as is shown by the extremely sharp orange PDF in the rightmost panel. Lower row: PDFs of velocity-integrated CO(1-0), [C I], [C II] (from left to right) intensities (K-km/s) in molecular and atomic gas. As we transition from molecular (CO 1-0) to atomic ([C I]) to ionized ([C II]) carbon emission, the fraction of emission that originates in molecular gas decreases, and the fraction that originates in atomic gas increases.

photons. It is clear from that the CO-dark factor depends strongly on N_{H} , which varies by several orders of magnitude in our simulations, and that it mildly depends on Z . One requires column densities of $\sim 3 \times 10^{21} \text{ cm}^{-2}$ before molecular clouds are CO-bright. Another way of saying this is that strongly CO-dark gas is typically relatively low column density.

In Figure 6, we show the probability distribution functions of gas density (n_{H}), H₂ abundances, column density (N_{H}) and kinetic temperature (T_{g}) for CO-dark and CO-bright molecular-dominated clouds. CO-dark gas is typically relatively diffuse (i.e. low volume or column density), warm ($> 10 \text{ K}$) and comprised of gas with relatively large H I mass fractions.

Taken together, these results paint a picture in which CO-dark molecular gas is typically lower column density, lower density, and in clouds with larger H I fractions overall than CO-bright gas. CO-bright gas, on the other hand, is typically quite dense ($n_{\text{H}} \gtrsim 50 \text{ cm}^{-3}$), cold ($T_{\text{g}} \sim 10 \text{ K}$), and highly extinct ($N_{\text{H}} \gtrsim 3 \times 10^{21} \text{ cm}^{-2}$).

5.3. What Is the Best Method for Tracing CO-dark Gas?

Having established both the quantity and physical properties of CO-dark gas, we now ask what the best method for tracing CO-dark gas is.

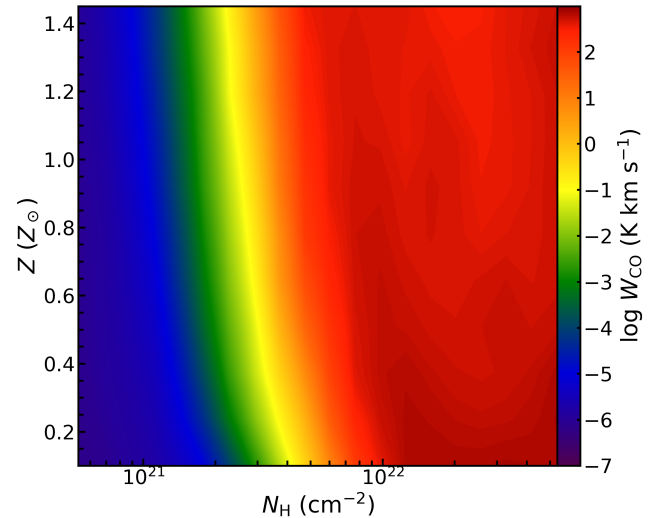


Figure 5. The CO(1-0) intensity of molecular gas of Halo 401 against column density (N_{H}) and metallicity (Z). The intensity increases as N_{H} and Z increase due to stronger dust shielding.

First, we want to know how luminous alternative tracers are in molecular gas. We show the [C II] and [C I] intensity of

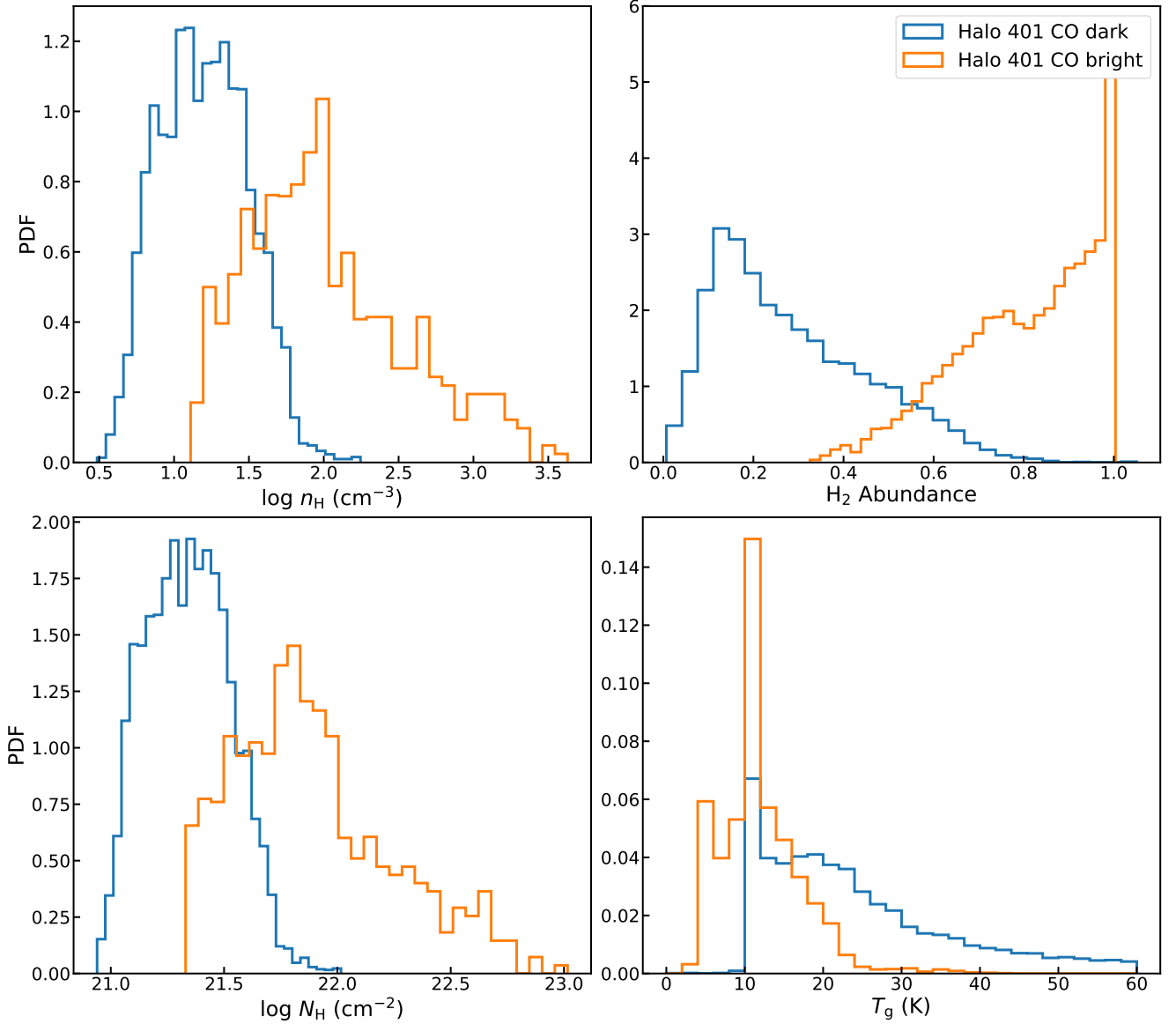


Figure 6. PDFs of gas density (n_{H} ; top left panel), H_2 abundances (top right panel), column density (N_{H} ; bottom left panel) and gas kinetic temperature (T_{g} , bottom right panel) for CO-dark (blue) and CO-bright (orange) gas. CO-bright gas is principally highly extinguished ($N_{\text{H}} \gtrsim 60 M_{\odot} \text{pc}^{-2}$), cold ($T_{\text{g}} \lesssim 10 \text{ K}$), dense gas ($n_{\text{H}} \gtrsim 50 \text{ cm}^{-3}$) with extremely high ($\gtrsim 60\%$) H_2 fractions across the whole cloud, while the CO-dark counterpart is mainly diffuse gas.

CO-dark gas and compare them to the CO-bright counterpart in Figure 7. The $[\text{C II}]$ intensity is brightest in the CO-dark gas, and negligible in CO-bright gas. At the same time, the $[\text{C I}]$ emission, while naturally brighter in the CO-dark gas, is also relatively bright even in the CO-bright gas. Note, the line intensity is approximately proportional to $\nu^3 T_{\text{b}}$ in typical molecular clouds, where ν is line center frequency and T_{b} is brightness temperature. Since $\nu_{[\text{C II}]}^3 / \nu_{[\text{C I}]}^3 = 57.6$, $[\text{C II}]$ has overall larger intensity than $[\text{C I}]$ in CO dark gas though $T_{\text{b},[\text{C I}]}$ is about twice as large as $T_{\text{b},[\text{C II}]}$.

We notice that, though $[\text{C II}]$ emission dominates in most of the CO-dark gas, $[\text{C I}]$ should also be strong enough to trace CO-dark gas (more than $\nu_{[\text{C I}]}^3 / \nu_{\text{CO}(1-0)}^3 = 78$ times as luminous as $\text{CO}(1-0)$ with $W_{\text{CO}} = 0.1 \text{ K-km/s}$ in general). Besides, $[\text{C II}]$ emission is generally too weak ($< 0.05 \text{ K km s}^{-1}$) to trace CO-bright gas while strong in the CO-dark counterpart. On the other hand, $[\text{C I}]$ emission is generally strong enough in CO-dark gas, while a range of intensities are found in CO-bright gas. This shows that $[\text{C I}]$ is capable of effectively tracing molecular gas with a wider range of properties than $[\text{C II}]$.

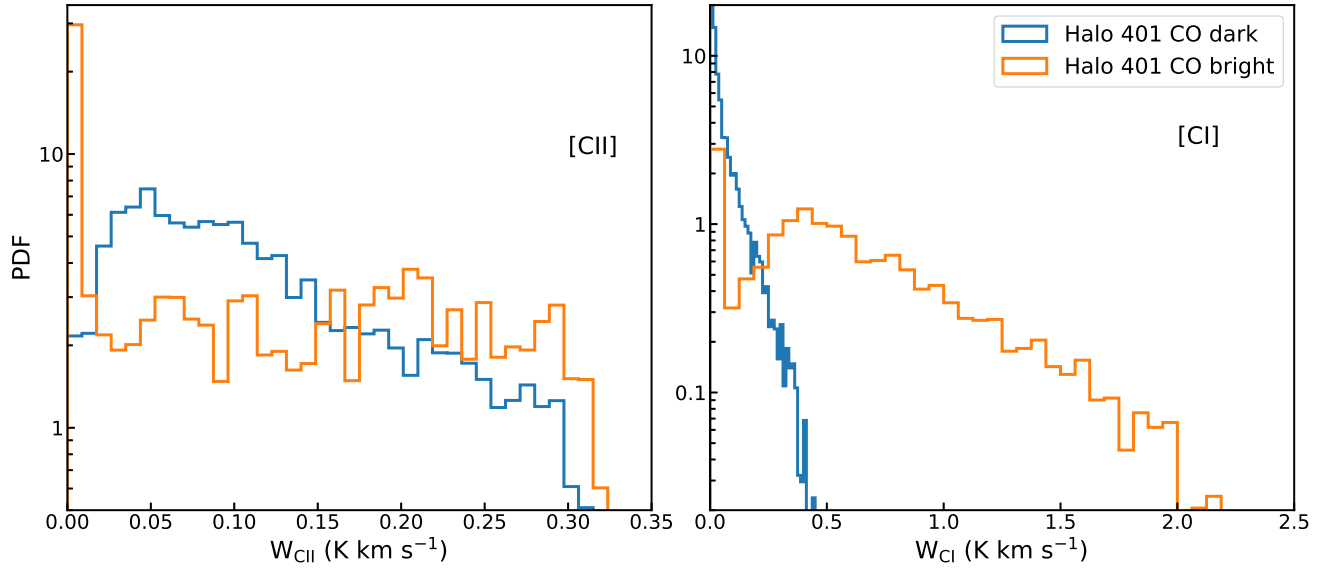


Figure 7. PDFs of Intensities of [C II] (left panel) and [C I] (right panel) emission from CO-dark (blue) and CO-bright (orange) gas. Strong emission of both [C II] and [C I] principally comes from CO-dark gas, while the emission is weak in CO-bright gas, especially for [C II]. Note, the line intensity is approximately proportional to $\nu^3 T_b$ in typical molecular clouds, where ν is line center frequency and T_b is brightness temperature. Since $\nu_{[C II]}^3/\nu_{[C I]}^3 = 57.6$, [C II] is overall more luminous than [C I] in CO dark gas.

After establishing the potentially effective tracers for CO dark gas, we now ask how we can use these tracers to determine the mass of underlying molecular gas. In other words, what are the [C I], [C II] and CO(1-0) conversion factors for CO bright and CO dark molecular gas?

In Figure 8, we evaluate the PDFs of the conversion factors for all H_2 with $W_{CO} > 10^{-5}$ K-km/s (see § 5; top), CO-dark H_2 (middle), and CO-bright H_2 (bottom); a significant amount of molecular gas is traced by all three tracers over all gas within central galaxies of Halo 401 and 352.

From the top panel we notice that there are two bumps for the X_{CO} PDF, revealing the impact of metal column density distribution and other secondary parameters. At the same time, distributions of X_{CI} and X_{CII} (especially X_{CI}) are relatively narrow with only one peak. The narrow distribution indicates that these two tracers are less sensitive to secondary parameters such as excitation, temperature, ISRF, and metallicity. Therefore these can reliably be used to trace the molecular gas in $z \sim 0$ disc galaxies.

Limiting the sample to CO-dark gas by our definition in § 5, we find that there is little change of X_{CI} and X_{CII} . The bimodal feature of X_{CO} , however, is shifted to a single bump. We therefore conclude that [C I] and [C II] perform better in tracing CO-dark molecular gas.

Shifting from CO-dark gas to the CO-bright counterpart, we find that the peak of X_{CI} PDF roughly remains unchanged and that the PDF becomes tighter. The peak of X_{CII} PDF, however, increases about 1 dex and deviates from the peak of X_{CII} PDF of all H_2 . This shows [C I], rather than [C II], remains a stable tracer over a wide range of physical properties.

6. DISCUSSION

6.1. How Much H_2 Is Traced at Different Intensity Thresholds?

We begin the discussion with Figure 9, where we show how much molecular gas can be traced by different carbon tracers above a different observed intensity thresholds. We use Halo 401 as an example, but note that Halo 352 has similar results. We focus on the solid lines here, and defer discussion about the dashed lines (in which we vary the cosmic ray ionization rate) to § 6.2.

From the solid lines in Figure 9, we see that at large integrated intensity values (e.g. $W_{C*} \sim 1$ K-km/s), the traced molecular gas is dominated by CO (1-0). In this regime, strong CO(1-0) comes from copious CO residing in highly shielded and extremely H_2 -rich gas, where C I and C^+ abundances are too low to generate strong emission. Even though strong [C II] and [C I] emission comes from diffuse molecular gas, the intensity is not at the same level as CO(1-0) from dense gas, due to the low gas density. At lower intensity thresholds, though, a much larger fraction of the gas is traced by [C I] and [C II] while CO(1-0) misses a significant amount of H_2 mass (e.g. $\sim 50\%$ missed at $W_{C*} \sim 0.1$ K-km/s), because most of the weak emission comes from diffuse molecular gas is CO-dark while [C I] and [C II]-luminous (see also § 4).

6.2. Sensitivity to Cosmic Ray Ionization

The cosmic ray ionization rate in galaxies is uncertain. Observations on diffuse molecular clouds (e.g. Wolfire et al. 2010; Indriolo et al. 2015; Neufeld et al. 2010; Neufeld & Wolfire 2017) and dense ones (McCall et al. 1999) within the Milky Way suggest rates that range from $\xi \sim 0.1 - 3 \times 10^{-16} \text{ s}^{-1}$. Because an increased cosmic ray ionization

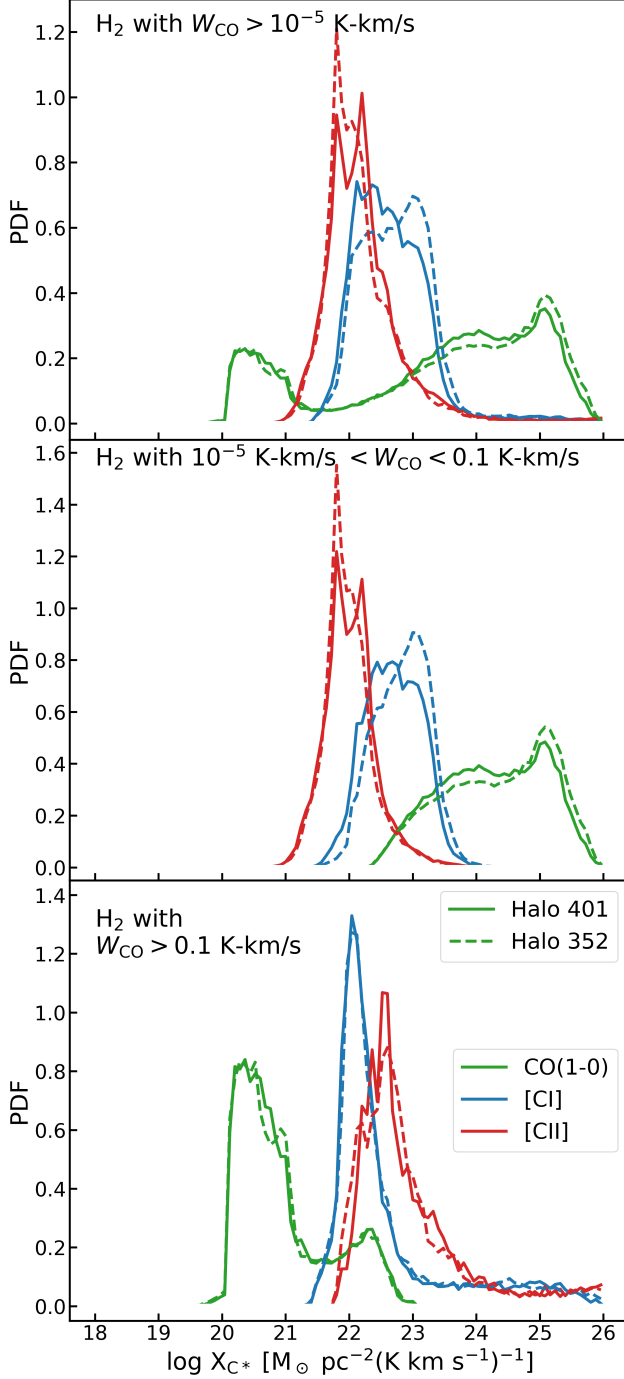


Figure 8. X_{CO} , X_{CI} and X_{CII} PDFs for Halo 401 and Halo 352. Top panel: PDFs for all H_2 with $W_{\text{CO}} > 10^{-5}$ K-km/s; we can see two bumps for $\text{CO}(1-0)$ and one bump for $[\text{C I}]$ and $[\text{C II}]$. The larger bump of the X_{CO} PDF mainly consists of CO -dark gas while the smaller CO -bright counterpart. Middle panel: PDFs for CO -dark gas (see § 5) for the definition. Bottom panel: PDFs for CO -bright gas. As is shown, the PDFs of X_{CI} and X_{CII} are much tighter than X_{CO} , implying weaker dependence on secondary parameters. $[\text{C I}]$ and $[\text{C II}]$ works better for CO -dark gas while the bimodal feature of X_{CO} PDF complicates the interpretation of $\text{CO}(1-0)$. X_{CI} , rather than X_{CII} , remains stable over a wide range of physical properties.

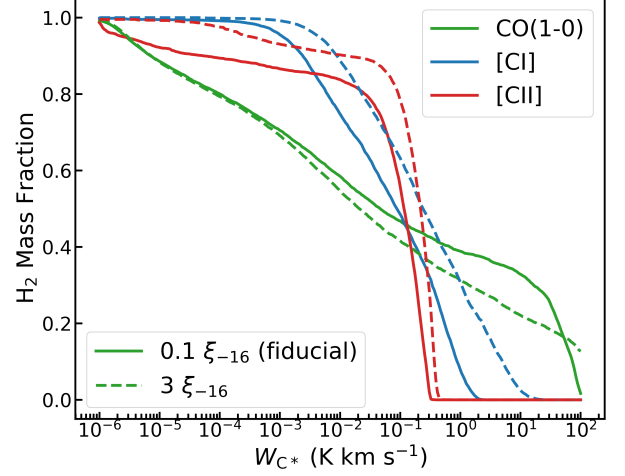


Figure 9. H_2 mass fraction traced by $\text{CO}(1-0)$, $[\text{C I}]$ and $[\text{C II}]$ as functions of intensity threshold (above which the emission can be detected) for Halo 401. At higher intensity threshold, the traced molecular gas is dominated by $\text{CO}(1-0)$. However, $\text{CO}(1-0)$ misses much of the molecular gas even with a very low threshold, and $[\text{C I}]$ and $[\text{C II}]$ take over. For example, at $W_{\text{CO}} \lesssim 0.1$ K-km/s, $\text{CO}(1-0)$ only traces a much smaller amount of H_2 mass, compared to $[\text{C I}]$ and $[\text{C II}]$. As shown by the dashed lines, where we artificially increase our cosmic ray ionization rate by a factor 30, this result is sensitive to the assumed cosmic ray ionization rate (further discussed in § 6.2).

rate can increase the fraction of dark gas (mainly via ionization of $\text{He} \rightarrow \text{He}^+$, and a subsequent 2 body reaction with CO), we therefore test the sensitivity of our results to the assumed value of ξ . Here, we adopt a relatively extreme normalization of $\xi = 3 \times 10^{-16} \text{ s}^{-1}$ for $\text{SFR} = 1 M_{\odot}/\text{yr}$ and compare the results to the fiducial case of $\xi \sim 0.1 \times 10^{-16} \text{ s}^{-1}$.

We return to Figure 9, but now highlight the dashed lines, in which we have assumed the larger ionization rate $\xi \sim 3 \times 10^{-16} \text{ s}^{-1}$. The mass fraction of molecular gas traced by $[\text{C II}]$ and $[\text{C I}]$ above specific intensity thresholds increases as CR ionization rate increases, while $\text{CO}(1-0)$ traces less molecular gas. This is a result of enhanced $[\text{C II}]$ and $[\text{C I}]$ abundances, as more CO is effectively destroyed by CR. The overall trend as discussed in § 6.1 remains unchanged, but the enhanced CR ionization potentially make $[\text{C II}]$ and $[\text{C I}]$ a better tracer of molecular gas.

We additionally check the effect of the normalization of CR ionization rate on the conversion factors, shown in Figure 10. We can see that $\text{CO}(1-0)$ performs even worse as a CO -bright H_2 tracer as the PDF of X_{CO} shows more power toward high X -factors (again, a result of increased dissociation of CO). $[\text{C I}]$ and $[\text{C II}]$ still perform well for CO -dark molecular gas. $[\text{C II}]$ still fails to trace part of diffuse gas as indicated by the shifting of the peak from top panel to bottom panel. Even if $[\text{C I}]$ is a still stable tracer of molecular

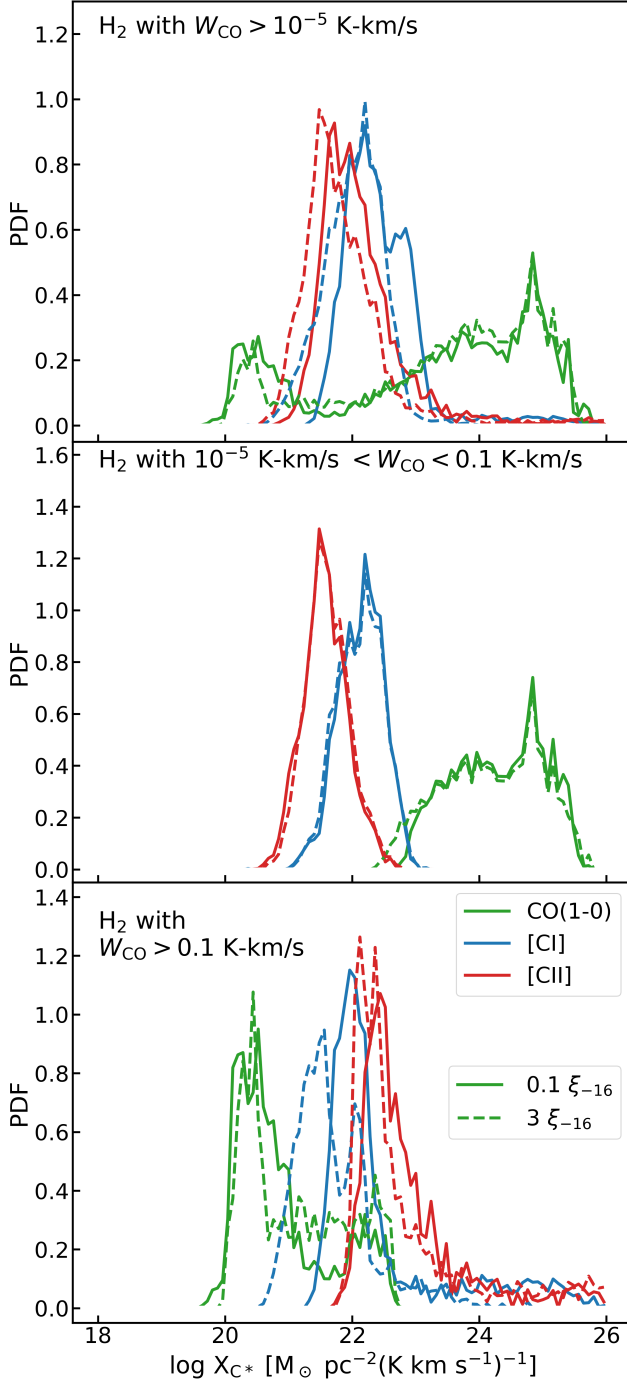


Figure 10. X_{CO} , X_{CI} and X_{CII} PDFs of Halo 401 for different normalization of cosmic ray ionization rates. Top panel: PDFs for all molecular gas with $W_{\text{CO}} > 10^{-5}$ K-km/s. Middle panel: PDFs for CO-dark molecular gas. Bottom panel: PDFs for CO-bright gas molecular gas.

gas with a wide range of physical properties, we notice, however, that the PDF of X_{CI} becomes ~ 1 dex wider and the median is ~ 0.5 dex smaller compared to the fiducial case. This said, while X_{CI} exhibits a relatively narrow distribution in values and remains stable across a wide range of physical properties, we caution that the typical value and the dispersion are relatively sensitive to the assumed normalization of the CR ionization rate.

We note, though, that these results may change as a result of the choice of chemical network. For example, [Gong et al. \(2017\)](#) find that the NL99+GC network may overestimate the effectiveness of cosmic rays in destroying CO, because it does not include grain-assisted recombination. This would suggest that the results presented here are best thought of as an upper limit as to the impact of cosmic rays. For comparison, in the Appendix we implement the [Gong et al. \(2017\)](#) chemical reaction network, and explore the impact of the cosmic ray ionization rate on our results. As we demonstrate in Figure 12, the usage of the Gong et al. network does not change our overall conclusions, but the PDFs of X -factors are less sensitive to the assumed CR ionization rate, as expected.

6.3. Comparing to Other Theoretical Work

Previous theoretical work (e.g. [Smith et al. 2014](#); [Glover & Smith 2016](#); [Gong et al. 2018](#)) on quantifying CO-dark molecular gas and alternative molecule tracers has typically been limited to studies of individual clouds or patches extracted from isolated galaxies. These studies define molecular gas as “CO-dark” if $W_{\text{CO}} < 0.1 \text{ K km s}^{-1}$. In particular, using a simulation of a patch of idealized Milky Way-like galaxy with a simplified on-the-fly chemical network, [Smith et al. \(2014\)](#) found $f_{\text{DG}} \sim 42\%$. In their simulation, a significant amount of CO-dark gas is located in long filaments which have low extinctions. They also show that the value of f_{DG} increase with increasing ISRF strength. Similarly, by post-processing 3D magnetohydrodynamics simulations of a kpc patch of galactic disks with solar neighborhood conditions, Meanwhile, [Gong et al. \(2018\)](#) find that f_{DG} is 26 – 79%, with the value of f_{DG} correlating with the average extinction of the simulated patch. [Gong et al. \(2018\)](#) also downgrade the spatial resolution of their synthetic CO maps and column density maps to various observational beam sizes, and find that in typical Galactic clouds, f_{DG} decreases with the increasing beam size because CO emission is smoothed out. [Gong et al. \(2018\)](#) estimate $f_{\text{DG}} \sim 50\%$ at the beam size $\sim 30 \text{ pc}$ which is similar to the minimum smoothing length of gas particles in the central galaxies of our zoom simulations at $z \sim 0$. Overall, our model gives a result consistent with previous work quantifying CO-dark molecular gas when using apples-to-apples metrics.

[Offner et al. \(2014\)](#) and [Glover et al. \(2015\)](#) compare [C I] against CO emission in simulations of a cloud-scale turbulent ISM. Contrary to the canonical view of C I as a “surface” tracer from simple 1-D PDR models (e.g. [Tielens & Hollenbach 1985](#); [Hollenbach & Tielens 1999](#)), their numerical studies show that C I can be prevalent in molecular clouds

with the help of turbulent “clumping” and turbulent diffusion. They point out several advantages of C I over CO, e.g. the column density regime of [C I] where the corresponding conversion factor X_{CI} remains approximately constant is larger, and X_{CI} is less sensitive to secondary parameters. Our simulations support these conclusions, and extend them to a far larger dynamic range in ISM conditions. We note, however, that our simulations lack the resolution to resolve the effect of clumping on the extinction of ISRF and the increased surface area exposed to ISRF in small scales. Still, we do consider the effect of sub-grid clumping on collisional thermal and chemical processes, and a simulation with $\epsilon \sim 25$ pc (close to $\epsilon \sim 30$ pc of our simulations), would have minimal sub-grid clumping effect on volume and column densities (Davé et al. 2016).

7. CONCLUSIONS

Combining cosmological hydrodynamic zoom-in galaxy formation simulations of $z \sim 0$ disc galaxies with thermal-radiative-chemical equilibrium interstellar ISM calculations, we investigate the utility of CO(1-0), [C I] and [C II] emission as molecular tracers in the environment of non-isolated galaxies. We summarize our main findings as following.

- Most CO(1-0), [C I] and [C II] emission comes from molecular gas, but as we transition from molecular (CO 1-0) to atomic ([C I]) to ionized ([C II]) carbon emission, the fraction of emission that originates in molecular gas decreases, and the fraction that originates in atomic gas increases.
- We define CO-dark gas as molecular gas. This criterion effectively distinguishes dense molecular gas from diffuse molecular gas. Using our definition

of CO-dark gas, we find that the CO-bright portion of the ISM consists principally of highly shielded ($N_{\text{H}} \gtrsim 200 M_{\odot} \text{ pc}^{-2}$) gas with extremely high densities ($n_{\text{H}} > 300 \text{ cm}^{-3}$) and H_2 abundances ($> 80\%$). As a result, observations that focus principally on CO can miss significant amounts of molecular gas.

- With our definition of CO-dark gas as the observationally motivated $W_{\text{CO}} < 0.1 \text{ K-km/s}$, the simulated disc galaxies have a significant amount ($\sim 53\%$) of CO-dark gas which can be traced by [C II] and [C I], emphasizing the importance of these tracers.
- We show the PDFs of CO(1-0), [C I] and [C II] conversion factors X_{CO} , X_{CI} and X_{CII} between observed line intensity and true H_2 column density. Of these, X_{CI} and X_{CII} tend to have a tighter distribution than X_{CO} , due to the sensitivity of CO (1-0) emission to secondary parameters such as metallicity.
- We find that [C I] is the overall preferable tracer of molecular gas within a wide range of physical properties. X_{CI} remains stable when shifted from CO-dark gas to CO-bright gas. [C I] is more luminous than CO(1-0) in CO-dark gas and bright in CO-bright gas, allowing it to trace a larger amount of H_2 mass.

Q.L. was funded by NSF grant AST-1724864. D.N. acknowledges funding from NSF grant AST-1724864, AST-1715206 and HST AR-13906.001 from the Space Telescope Science Institute. M.R.K. acknowledges support from the Australian Research Council’s Discovery Projects funding scheme, grant DP160100695.

APPENDIX

In order to determine the sensitivity of our results to our choice of chemical network, in this appendix we repeat some of the key calculations in the paper using the Gong et al. (2017) chemical network instead of our fiducial NL99+GC network.

A. CHEMICAL STRUCTURES OF A TYPICAL CLOUD

We show in Figure 11 the chemical structures (i.e. radial profiles) of a typical molecular cloud with $n_{\text{H}} = 105.87 \text{ cm}^{-3}$, $N_{\text{H}} = 149.26 M_{\odot} \text{ pc}^{-2}$, $Z' = 1.04$, and $\text{SFR} = 1 M_{\odot}/\text{yr}$. We adopt here the CR ionization rate $\xi = 10^{-17} \text{ s}^{-1}$. We notice that the grain-catalyzed recombination incorporated in Gong et al. (2017) network leads to a significantly higher [C I] and CO(1-0) intensities in the outer layers ($N_{\text{H}} \leq 40 M_{\odot} \text{ pc}^{-2}$) where the ionization via CRs and energetic ISRF is strong.

B. CONVERSION FACTORS OF THREE CARBON-BASED TRACERS

We show in Figure 12 the PDFs of X_{CO} , X_{CI} and X_{CII} of Halo 401 for two different cosmic ray ionization rates, using Gong et al. (2017) networks. Comparing the result to the previous discussion in § 6.2, the inclusion of grain-catalyzed recombination does not change our overall conclusions.

C. RESOLUTION TESTS

We show in Figure 13 the PDFs of X_{CO} , X_{CI} and X_{CII} of Halo 401 for models with different number of layers ($N_{\text{zone}} = 8, 16, 32$ and 64). The tests utilize a cruder grid, the spacing of which is 0.28, 0.4 dex, 0.4 dex, 0.3 dex for Z' , n_{H} , N_{H} and SFR respectively. The differences are minor.

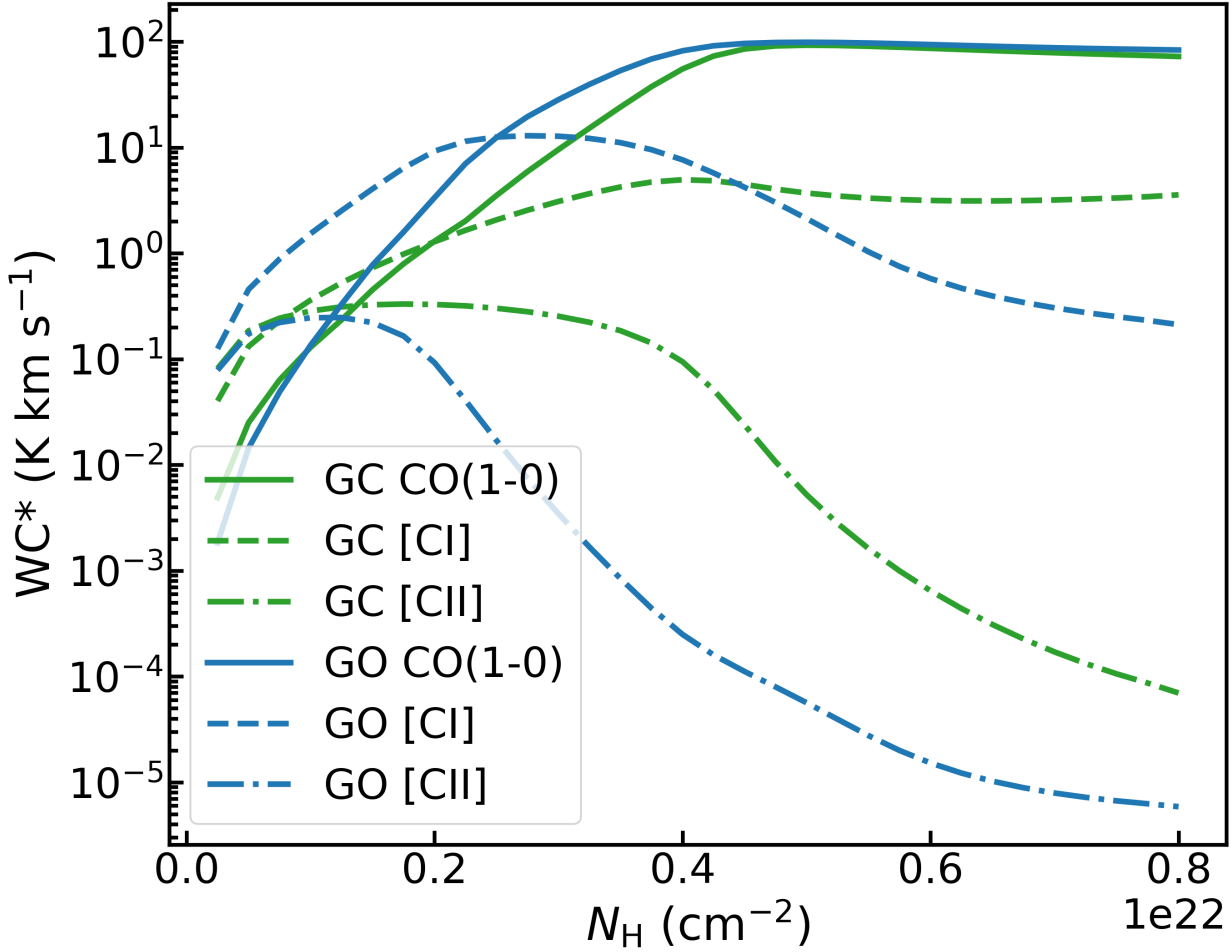


Figure 11. CO(1-0) (solid line), [C I] (dashed line) and [C II] (dotted line) intensity as a function of N_H for a radially stratified gas particle with $n_H = 105.87 \text{ cm}^{-3}$, $N_H = 149.26 M_\odot \text{ pc}^{-2}$, $Z' = 1.04$, and $\text{SFR} = 1 M_\odot/\text{yr}$, using the Gong et al. (2017) network (blue) and our fiducial NL99+GC network (green), respectively

REFERENCES

- Abruzzo, M. W., Narayanan, D., Davé, R., & Thompson, R. 2018, arXiv/1803.02374, arXiv:1803.02374
- Accurso, G., Saintonge, A., Bisbas, T. G., & Viti, S. 2017, MNRAS, 464, 3315
- Asplund, M., Grevesse, N., Sauval, A. J., & Scott, P. 2009, ARA&A, 47, 481
- Barinova, Ğ., van Hemert, M. C., Krems, R., & Dalgarno, A. 2005, ApJ, 620, 537
- Bell, T. A., Viti, S., & Williams, D. A. 2007, MNRAS, 378, 983
- Bisbas, T. G., Papadopoulos, P. P., & Viti, S. 2015, ApJ, 803, 37
- Bolatto, A. D., Wolfire, M., & Leroy, A. K. 2013, ARA&A, 51, 207
- Bothwell, M. S., Aguirre, J. E., Aravena, M., et al. 2017, MNRAS, 466, 2825
- Bruzual, G., & Charlot, S. 2003, MNRAS, 344, 1000
- Casey, C. M., Narayanan, D., & Cooray, A. 2014, Physics Reports, 541, 45
- Chabrier, G. 2003, PASP, 115, 763
- Chomiuk, L., & Povich, M. S. 2011, AJ, 142, 197
- Cubick, M., Stutzki, J., Ossenkopf, V., Kramer, C., & Röllig, M. 2008, A&A, 488, 623
- Davé, R., Rafieeferantsoa, M. H., & Thompson, R. J. 2017a, arXiv/1704.01335, arXiv:1704.01135
- Davé, R., Rafieeferantsoa, M. H., Thompson, R. J., & Hopkins, P. F. 2017b, MNRAS, arXiv:1610.01626

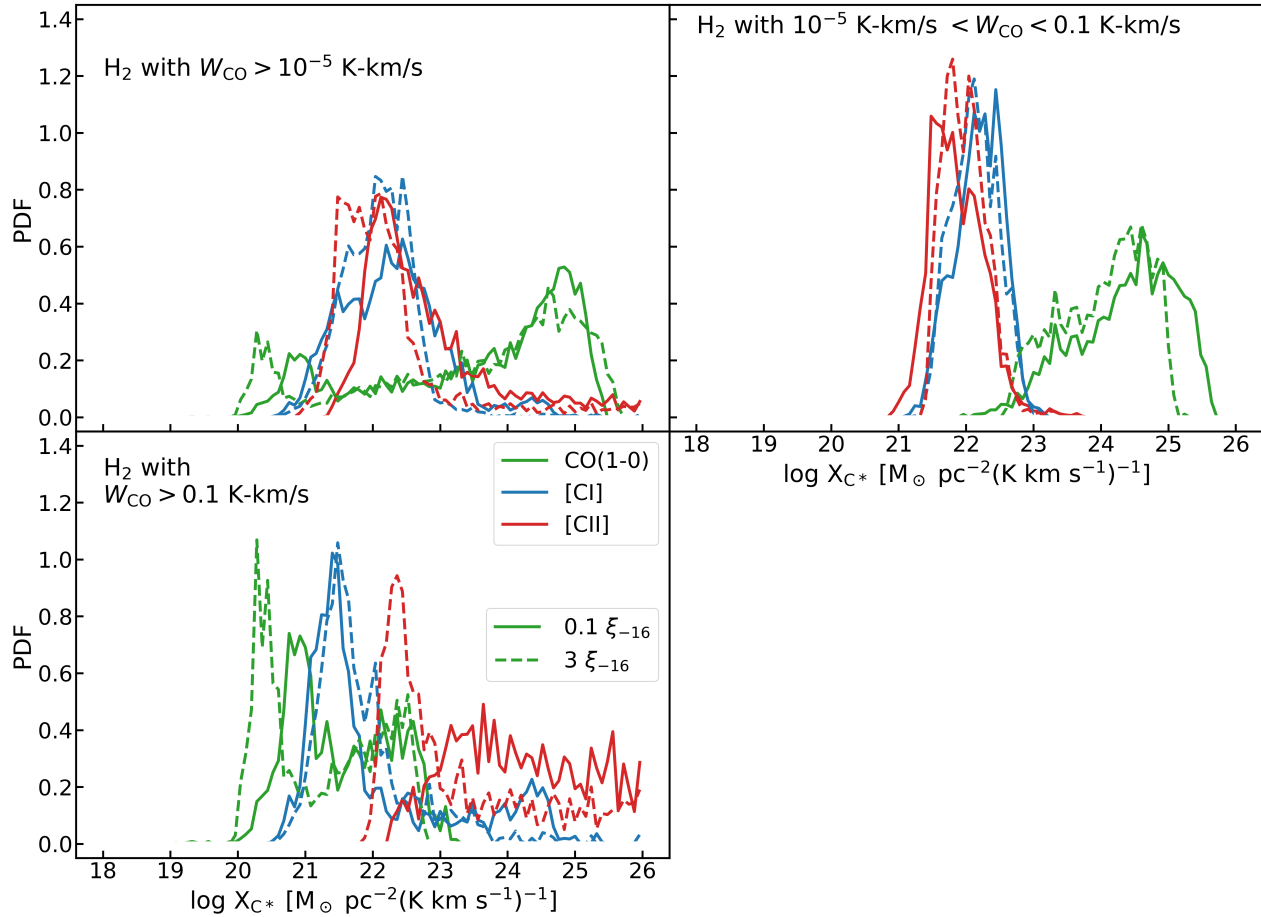


Figure 12. X_{CO} , X_{CI} and X_{CII} PDFs of Halo 401 for different cosmic ray ionization rates, computed using the Gong et al. (2017) network. Top-left panel: PDFs for all molecular gas with $W_{\text{CO}} > 10^{-5}$ K-km/s. Top-right panel: PDFs for CO-dark gas by our definition (see § 5). Bottom-left panel: PDFs for CO-bright gas.

Davé, R., Thompson, R., & Hopkins, P. F. 2016, MNRAS, 462, 3265

Draine, B. T. 2011, Physics of the Interstellar and Intergalactic Medium (Princeton University Press: Princeton, NJ)

Draine, B. T., & Bertoldi, F. 1996, ApJ, 468, 269

Feldmann, R., Gnedin, N. Y., & Kravtsov, A. V. 2012, ApJ, 747, 124

Flower, D. R. 1988, Journal of Physics B Atomic Molecular Physics, 21, L451

—. 2001, Journal of Physics B Atomic Molecular Physics, 34, 2731

Flower, D. R., & Launay, J. M. 1977, Journal of Physics B Atomic Molecular Physics, 10, 3673

Glover, S. C. O., Clark, P. C., Micic, M., & Molina, F. 2015, MNRAS, 448, 1607

Glover, S. C. O., & Mac Low, M.-M. 2007, ApJS, 169, 239

Glover, S. C. O., & Smith, R. J. 2016, MNRAS, 462, 3011

Goldsmith, P. F. 2001, ApJ, 557, 736

Goldsmith, P. F., Langer, W. D., Pineda, J. L., & Velusamy, T. 2012, ApJS, 203, 13

Gong, M., Ostriker, E. C., & Kim, C.-G. 2018, ArXiv e-prints, arXiv:1803.09822

Gong, M., Ostriker, E. C., & Wolfire, M. G. 2017, ApJ, 843, 38

Grenier, I. A., Casandjian, J.-M., & Terrier, R. 2005, Science, 307, 1292

Hahn, O., & Abel, T. 2011, MNRAS, 415, 2101

Herrera-Camus, R., Bolatto, A. D., Wolfire, M. G., et al. 2015, ApJ, 800, 1

Heyer, M., Gutermuth, R., Urquhart, J. S., et al. 2016, A&A, 588, A29

Hollenbach, D. J., & Tielens, A. G. G. M. 1999, Reviews of Modern Physics, 71, 173

Hopkins, P. F. 2015, MNRAS, 450, 53

—. 2017, arXiv/1712.01294, arXiv:1712.01294

Hopkins, P. F., Kereš, D., Oñorbe, J., et al. 2014, MNRAS, 445, 581

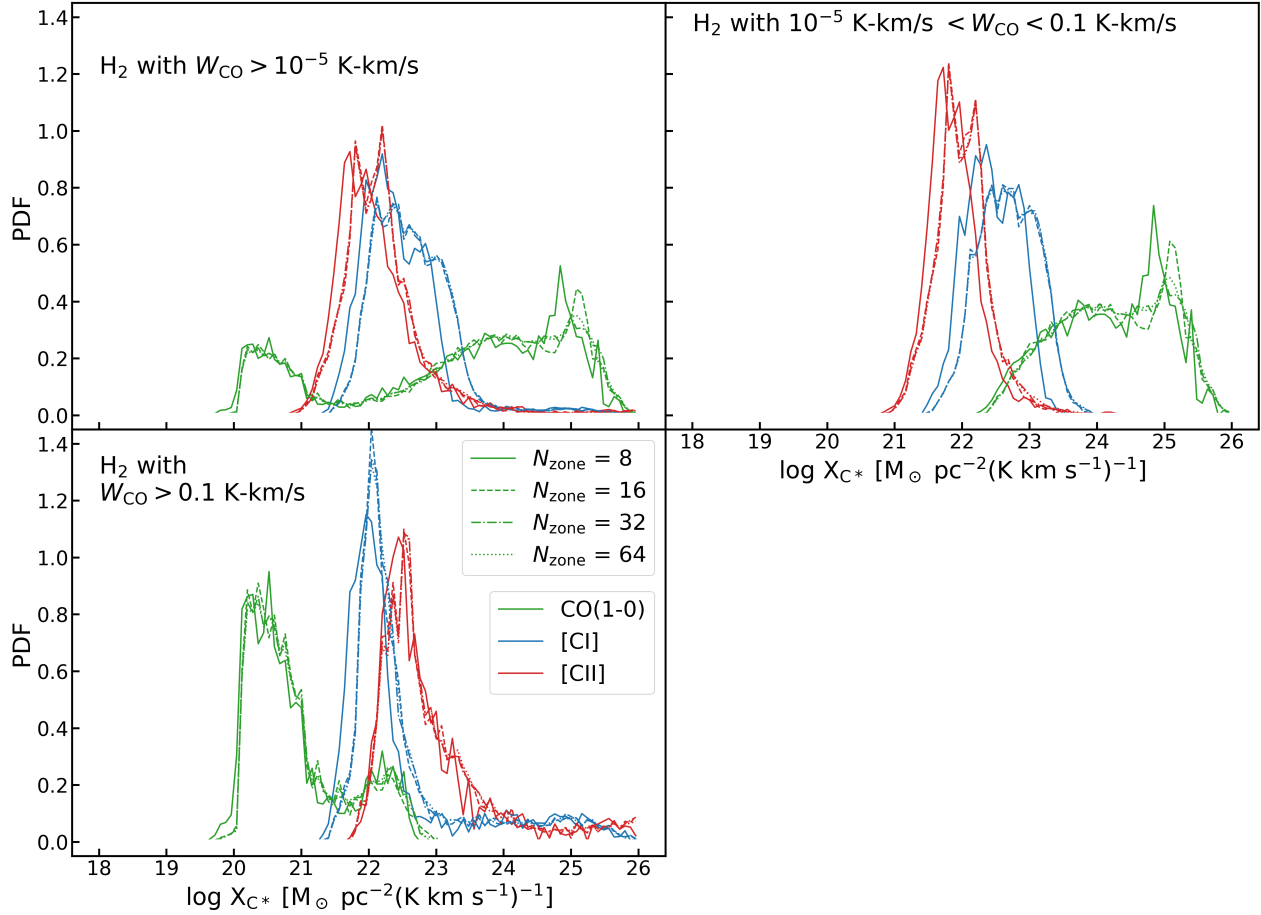


Figure 13. Convergence tests show X_{CO} , X_{CI} and X_{CII} PDFs of Halo 401 for models with different number of layers ($N_{\text{zone}} = 8, 16, 32$ and 64), computed using the NL99+GC network and fiducial cosmic ray ionization rates $\xi = 10^{-17} \text{ SFR}/M_{\odot} \text{ yr}^{-1} \text{ s}^{-1}$. Top-left panel: PDFs for all molecular gas with $W_{\text{CO}} > 10^{-5} \text{ K-km/s}$. Top-right panel: PDFs for CO-dark gas by our definition (see § 5). Bottom-left panel: PDFs for CO-bright gas.

Hopkins, P. F., Wetzel, A., Keres, D., et al. 2017, arXiv/1702.06148, arXiv:1702.06148

Indriolo, N., Neufeld, D. A., Gerin, M., et al. 2015, ApJ, 800, 40

Israel, F. P., Rosenberg, M. J. F., & van der Werf, P. 2015, A&A, 578, A95

Iwamoto, K., Brachwitz, F., Nomoto, K., et al. 1999, ApJS, 125, 439

Jankowski, P., & Szalewicz, K. 2005, JChPh, 123, 104301

Johnson, C. T., Burke, P. G., & Kingston, A. E. 1987, Journal of Physics B Atomic Molecular Physics, 20, 2553

Kennicutt, R. C., & Evans, N. J. 2012, ARA&A, 50, 531

Kennicutt, Jr., R. C. 1998, ARA&A, 36, 189

Krumholz, M. R. 2014, PhR, 539, 49

Krumholz, M. R., Dekel, A., & McKee, C. F. 2012, ApJ, 745, 69

Krumholz, M. R., Leroy, A. K., & McKee, C. F. 2011, ApJ, 731, 25

Krumholz, M. R., McKee, C. F., & Tumlinson, J. 2009, ApJ, 693, 216

Kudritzki, R.-P., Urbaneja, M. A., Gazak, Z., et al. 2012, ApJ, 747, 15

Kuhlen, M., Krumholz, M. R., Madau, P., Smith, B. D., & Wise, J. 2012, ApJ, 749, 36

Lada, C. J., & Lada, E. A. 2003, ARA&A, 41, 57

Langer, W. D., Pineda, J. L., & Velusamy, T. 2014a, A&A, 564, A101

Langer, W. D., Velusamy, T., Pineda, J. L., Willacy, K., & Goldsmith, P. F. 2014b, A&A, 561, A122

Launay, J.-M., & Roueff, E. 1977, Journal of Physics B Atomic Molecular Physics, 10, 879

Lee, H., Bettens, R. P. A., & Herbst, E. 1996, A&AS, 119, 111

Leroy, A. K., Hughes, A., Schrubba, A., et al. 2016, ApJ, 831, 16

Leroy, A. K., Schinnerer, E., Hughes, A., et al. 2017, ApJ, 846, 71

Lique, F., Werfelli, G., Halvick, P., et al. 2013, JChPh, 138, 204314

McCall, B. J., Geballe, T. R., Hinkle, K. H., & Oka, T. 1999, ApJ, 522, 338

- Muratov, A. L., Kereš, D., Faucher-Giguère, C.-A., et al. 2015, *MNRAS*, 454, 2691
- Narayanan, D., Conroy, C., Dave, R., Johnson, B., & Popping, G. 2018a, arXiv/1805.06905, arXiv:1805.06905
- Narayanan, D., & Davé, R. 2012, *MNRAS*, 423, 3601
- Narayanan, D., Davé, R., Johnson, B. D., et al. 2018b, *MNRAS*, 474, 1718
- Narayanan, D., Krumholz, M., Ostriker, E. C., & Hernquist, L. 2011, *MNRAS*, 418, 664
- Narayanan, D., & Krumholz, M. R. 2017, *MNRAS*, 467, 50
- Narayanan, D., Krumholz, M. R., Ostriker, E. C., & Hernquist, L. 2012, *MNRAS*, 421, 3127
- Nelson, R. P., & Langer, W. D. 1999, *ApJ*, 524, 923
- Neufeld, D. A., & Wolfire, M. G. 2017, *ApJ*, 845, 163
- Neufeld, D. A., Goicoechea, J. R., Sonnentrucker, P., et al. 2010, *A&A*, 521, L10
- Nomoto, K., Tominaga, N., Umeda, H., Kobayashi, C., & Maeda, K. 2006, *Nuclear Physics A*, 777, 424
- Offner, S. S. R., Bisbas, T. G., Bell, T. A., & Viti, S. 2014, *MNRAS*, 440, L81
- Olsen, K., Greve, T. R., Narayanan, D., et al. 2017, *ApJ*, 846, 105
- Olsen, K. P., Greve, T. R., Narayanan, D., et al. 2015, *ArXiv e-prints*, arXiv:1507.00362
- Oppenheimer, B. D., & Davé, R. 2006, *MNRAS*, 373, 1265
- Papadopoulos, P. P., & Greve, T. R. 2004, *ApJL*, 615, L29
- Papadopoulos, P. P., Thi, W.-F., & Viti, S. 2004, *MNRAS*, 351, 147
- Pineda, J. E., Caselli, P., & Goodman, A. A. 2008, *ApJ*, 679, 481
- Pineda, J. L., Langer, W. D., & Goldsmith, P. F. 2014, *A&A*, 570, A121
- Pineda, J. L., Langer, W. D., Velusamy, T., & Goldsmith, P. F. 2013, *A&A*, 554, A103
- Planck Collaboration, Ade, P. A. R., Aghanim, N., et al. 2011, *A&A*, 536, A19
- Privon, G. C., Narayanan, D., & Davé, R. 2018, arXiv/1805.03649, arXiv:1805.03649
- Ripple, F., Heyer, M. H., Gutermuth, R., Snell, R. L., & Brunt, C. M. 2013, *MNRAS*, 431, 1296
- Robitaille, T. P., & Whitney, B. A. 2010, *ApJL*, 710, L11
- Roueff, E., & Le Bourlot, J. 1990, *A&A*, 236, 515
- Schmidt, M. 1959, *ApJ*, 129, 243
- Schöier, F. L., van der Tak, F. F. S., van Dishoeck, E. F., & Black, J. H. 2005, *A&A*, 432, 369
- Schroder, K., Staemmler, V., Smith, M. D., Flower, D. R., & Jaquet, R. 1991, *Journal of Physics B Atomic Molecular Physics*, 24, 2487
- Shetty, R., et al. 2011a, *MNRAS*, 412, 1686
- . 2011b, *MNRAS*, 415, 3253
- Smith, B. D., Bryan, G. L., Glover, S. C. O., et al. 2017, *MNRAS*, 466, 2217
- Smith, M. W. L., Eales, S. A., Gomez, H. L., et al. 2012, *ApJ*, 756, 40
- Smith, R. J., Glover, S. C. O., Clark, P. C., Klessen, R. S., & Springel, V. 2014, *MNRAS*, 441, 1628
- Spaans, M., & van Dishoeck, E. F. 1997, *A&A*, 323, 953
- Staemmler, V., & Flower, D. R. 1991, *Journal of Physics B Atomic Molecular Physics*, 24, 2343
- Thompson, R., Nagamine, K., Jaacks, J., & Choi, J.-H. 2014, *ApJ*, 780, 145
- Tielens, A. G. G. M., & Hollenbach, D. 1985, *ApJ*, 291, 722
- Tremonti, C. A., Heckman, T. M., Kauffmann, G., et al. 2004, *ApJ*, 613, 898
- van Dishoeck, E. F., & Black, J. H. 1988, *ApJ*, 334, 771
- Vutisalchavakul, N., Evans, II, N. J., & Heyer, M. 2016, *ApJ*, 831, 73
- Walter, F., Weiß, A., Downes, D., Decarli, R., & Henkel, C. 2011, *ApJ*, 730, 18
- Wernli, M., Valiron, P., Faure, A., et al. 2006, *A&A*, 446, 367
- Wiesenfeld, L., & Goldsmith, P. F. 2014, *ApJ*, 780, 183
- Wilson, N. J., & Bell, K. L. 2002, *MNRAS*, 337, 1027
- Wolfire, M. G., Hollenbach, D., & McKee, C. F. 2010, *ApJ*, 716, 1191
- Xie, T., Allen, M., & Langer, W. D. 1995, *ApJ*, 440, 674
- Yang, B., Stancil, P. C., Balakrishnan, N., & Forrey, R. C. 2010, *ApJ*, 718, 1062